Geophysical Journal International

Geophys. J. Int. (2026) **244,** 1–11
Advance Access publication 2025 November 26
Research Paper

https://doi.org/10.1093/gji/ggaf482

Muography for structural characterization of volcanoes: a case study at Mount Unzen, Japan

László Oláh [1,2] László Tercsi,[2] Dezső Varga,[1,2] Hiroyuki K. M. Tanaka,[1,3] Seiki Kubo,[4] Sinya Yoshida,[4] Kazumichi Iwata,[4] Junichi Akanuma,[5] Masafumi Kaneko[5] and Hisashi Watanabe [5]

[1] *International Virtual Muography Institute (VMI), 1-1-1 Yayoi, Bunkyo-ku, Tokyo 113-0032, Japan*
[2] *Institute for Particle and Nuclear Physics, HUN-REN Wigner Research Centre for Physics, Hungarian Research Network, 29-33 Konkoly-Thege Miklós Str., Budapest 1121, Hungary. E-mail: olah.laszlo@wigner.hu*
[3] *Earthquake Research Institute, The University of Tokyo, 1-1-1 Yayoi, Bunkyo-ku, Tokyo 113-0032, Japan*
[4] *Unzen Sabo Management Center, Kyushu Regional Development Bureau, Ministry of Land, Infrastructure, Transport and Tourism, Minamishimokawashirimachi, Shimabara, Nagasaki 855-0866, Japan*
[5] *Sabo Frontier Foundation (SFF), SABO-Kaikan, Annex 6F, 2-7-4, Hirakawacho, Chiyoda-ku, Tokyo 102-0093, Japan*

Accepted 2025 November 21. Received 2025 November 17; in original form 2025 September 1

SUMMARY

Destabilization of volcanic edifices can generate debris avalanches with catastrophic impacts on their environment. We present the first high-resolution muography of Mount Unzen, Japan, conducted to characterize the structure of lava lobes formed on the volcano's summit and flank during the 1990–1995 eruption. A multi-wire-proportional-chamber-based muon tracking system was operated for 203 d. The obtained high-resolution muographic image shows the internal density structure of Mount Unzen with a spatial resolution of 12 m. Mean densities were respectively measured as 2470 and 2290 kg m^{-3} for the base rock and a fracture zone, and both were consistent with the results of prior drilling and sampling experiments. The mean density of lava lobes was measured significantly lower value of 1570 kg m^{-3}, indicating post-eruptive structural weakening. A comparison between the time-series of muographically measured density-lengths and daily precipitation records suggest that rainfall-induced gravitational destabilization did not occur during the observational period. This work demonstrates that long-term (multi-year) muon monitoring of the lava lobes can provide valuable complementary information for volcanic stability assessments.

Key words: Japan; Image processing; Instability analysis; Volcanic hazards and risks; Volcaniclastic deposits; Volcano monitoring.

1. INTRODUCTION

Failures of volcanic slopes can result in the partial collapse of edifices, generating debris avalanches which can run out within a distance of a few tens of kilometres (Voight & Elsworth 1997; Voight 2000). Volcanic avalanches are often accompanied by active volcanism, either magmatic explosive eruptions (Voight *et al.* 1983) or phreatic explosive eruptions (Siebert *et al.* 1987). However, some avalanches are generated without volcanic activity due to gradual spreading of the volcano basement (van Wyk de Vries & Francis 1997). The causal processes are direct effects of subsurface magma evolution and movement (McGuire *et al.* 1990), indirect effects of magma that increase the pressure of pore fluids (Reid 2004; Heap *et al.* 2021a), which decrease rocks frictional resistance (Elsworth & Voight 2001) and cause hydrothermal alteration (López & Williams 1993; Heap *et al.* 2021b) and fracturing that reduce the strength of both altered and hosting rocks, and seismic shaking of the edifice (Giudicepietro *et al.* 2023). Collapses are rather triggered by a combination of the different processes and circumstances instead of individuals (Voight & Elsworth 1997).

Structural stability analysis of volcanic slopes and predicting future debris avalanches are complex tasks that require integrating several approaches; including analysing past events, studying avalanches in analogous volcanic setting, conducting material characterization experiments and applying geophysical monitoring techniques for structural characterization (Voight 2000; Peruzzetto *et al.* 2019; Heap & Violay 2021). The material characterization experiments are applied for assessing the rock strength (Darmawan *et al.* 2022). Typically an order of magnitude difference is observed in rock strength and 500–1000 kg m^{-3} in bulk density between hydrothermally altered and host rocks (Watters *et al.* 2000). It is crucial to identify appropriate zones of volcanic edifice where samples can

be collected for the laboratory tests. Moreover, a limitation of laboratory testing of rock samples is that it is practically impossible to test sufficient volumes of the rock mass to characterize the volcanic edifice (Poganj *et al.* 2025). Geophysical surveying techniques (e.g. Rosas Carbajal *et al.* 2016; Byrdina *et al.* 2017) explore the weak zones in volcanoes and localize where to collect the samples for the rock strength analysis. However, volcanic activities and geographical features can make the volcanic edifices inaccessible and hamper the surveying by the geophysical techniques. Airborne optical imagery techniques, such as drone-based optical photogrammetry (e.g. Darmawan *et al.* 2018) or satellite imagery (Pallister *et al.* 2019; Dumont *et al.* 2022), are utilized for remote monitoring of inaccessible volcanic edifices. The optical photogrammetry allows monitoring of geothermal activities (Oppenheimer *et al.* 1993) and provides qualitative indication of alteration and sulfuric deposition besides structural information (Müller *et al.* 2021). However, the pixel size of satellite imagery allows a spatial resolution of a few tens of metres that is not a sufficient resolution to observe the evolution of alteration at lava domes. Furthermore, limited visibility caused by weather conditions can hinder the application of airborne techniques. Ground surface deformation monitoring by Global Positioning System and Interferometric Synthetic Aperture Radars (InSAR) revealed subsurface magma intrusions as causative processes of flank destabilization (e.g. Puglisi *et al.* 2008; Schaefer *et al.* 2019). Ground-Based Synthetic Aperture Radar were also utilized at a few volcanic edfices, for example, at Mount Unzen, Japan (Daikai *et al.* 2024), to reduce periodic time of observations from a few days to a few minutes for flank stability assessment. The causative subsurface processes of ground surface deformations are not always known that limits the reliability of hazard assessment (Biggs *et al.* 2014). Mass density sensitive techniques are required to observe the movement and evolution of materials either deposited on the flank or located beneath the surface. In this work, we applied muography to aid the limitations of the aforementioned techniques.

Muography is a passive, non-destructive and remote imaging technique that quantifies the amount of materials and their evolution over time in large-sized structures (e.g. Lesparre *et al.* 2010; Tanaka *et al.* 2023). The muographic image processing is based on measuring the directional dependent yield of penetrated atmospheric muon particles with tracking detectors operated around or beneath the scanned structures. The high penetrating power and small deflections of muons allow muographic imaging with an angular resolution of a few milliradians. These advantages make muography a useful complementary monitoring technique in geophysics and geotechnics (Zhang *et al.* 2020; Lechmann *et al.* 2021). Muon tomography (e.g. Nagahara *et al.* 2022) and joint inversion of muographic and gravimetric data (e.g. Nishiyama *et al.* 2017) improved the spatial resolution of subsurface exploration to a few metres. Integrated processing of muographic and seismic data enabled the determination of physical constants of rock samples (Matsushima *et al.* 2024). Combining muography and ground surface deformation monitoring identified and localized ground deformation sources (Oláh *et al.* 2023). However, muons' yield is about 160 per square meter per second at sea level and it decreases significantly (approx. 3–4 orders of magnitude) after a few hundred metres of materials (Lesparre *et al.* 2010; Lechmann *et al.* 2018). Consequently, collecting sufficient number of muons for scanning of mountain-sized structures requires a relatively long measurement time (from a few months to a few years) even with large-sized or modular muographic observation system (MOS). Muography has successfully been applied for exploration of ore bodies (e.g. Schouten 2019; Liu *et al.* 2024) and for searching hidden geological hazards created

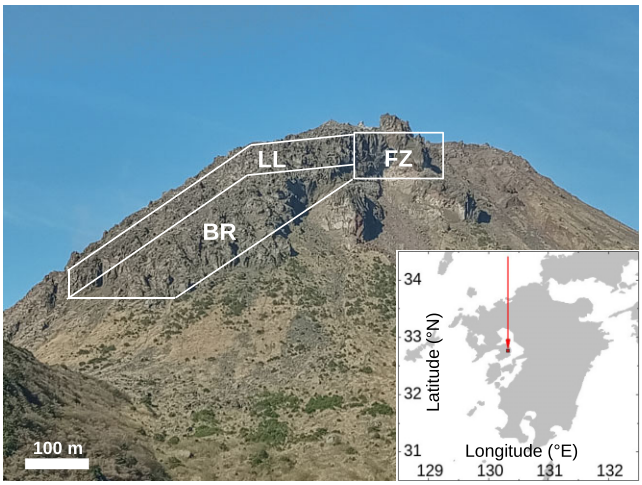

Figure 1. A photograph of Mount Unzen is shown. White lines designate the studied parts of the volcanic edifice. The base rock (BR) represents the volcanic edifice before the eruption of 1990–1995. A fracture zone (FZ) involves the upper conduit and the vent. The lava lobes (LL) were released onto the summit and the flank during the eruption of 1990–1995. The internal map shows the location of the measurement site (rectangle) in Kyushu, Japan.

by either nature (Athanassas 2020; Balázs *et al.* 2024) or human activities (Holma *et al.* 2022; Beni *et al.* 2025). Volcanoes have also been studied with muography for measuring the conduit structures and monitoring magmatic materials (Carbone *et al.* 2013; Portal *et al.* 2013; Tanaka 2019; Macedonio *et al.* 2022; Oláh *et al.* 2023), hydrothermal processes (Rosas-Carbajal *et al.* 2017; Gibert *et al.* 2022), tectonic changes (Miyamoto *et al.* 2010; Lo Presti *et al.* 2020), volcanic ash deposition and erosion processes (Oláh *et al.* 2021), etc. Here we focus on the muography of Mount Unzen to characterize its structure and provide complementary information for structural stability analysis.

2. GEOLOGICAL SETTING AND SITE CHARACTERIZATION

Mount Unzen is a stratovolcano that consists of a group of lava domes on the Shimabara Peninsula, Kyushu, Japan. This volcanic complex is fed with magma from the Chijiwa Caldera located beneath the Tachibana Bay. The inner map of Fig. 1 shows the location of Mount Unzen (red-coloured rectangle) in Kyushu, Japan. The photograph of Fig. 1 shows Mount Unzen from the muography observatory. Three zones of volcanic edifice were selected for our study based on the geologic maps created in earlier works (Nakada *et al.* 1999; Hirakawa et al. 2018): the fracture zone (FZ) around the upper conduit of Fugendake crater, a part of the base rock (BR), and the viscous lava lobes (LL) built from 2.1×10^8 m^3 of dacite magma released onto the base rock by the eruptions of 1990–1995 (Sato *et al.* 1992; Yamamoto *et al.* 1993; Nakada *et al.* 1999). The density of lava lobes reduced by ramp structure formation due to gravitational lava flow, resulting in a highly porous, low-density talus. Syn-eruptive gravitational collapses of the lava lobes induced pyroclastic density flows that killed more than 40 people, and post-eruptive rain-triggered debris flows have also resulted in serious economic losses. By the end of the eruption period, the lateral sizes of the lava lobes extended 1200 m in the east–west direction and 800 m in the north–south direction, and its height reached 130 m.

The eruption period was ended by spine extrusion onto the summit (Hornby *et al.* 2015).

The internal structures of the plumbing system and the lava lobes have intensively been studied since the last eruption. We highlight a few achievements and findings without claiming completeness as follows. In 2004, the Unzen Scientific Drilling Project (USDP) reached the lava dike that fed the 1991–1995 eruption about 1500 m beneath the summit (Nakada *et al.* 2005). Here the temperatures were measured significantly lower than expected, *ca.* 420 °K instead of *ca.* 1070 °K, which suggested the cooling of the lava dike by hydrothermal circulation. Post-eruptive time-lapse gravity investigations indicated the occurrence of ground water recharge and hydrothermal circulation from 1999 to 2004 (Saibi *et al.* 2010). These shallow hydrological processes induced the alteration of the volcanic rocks (e.g. Heap *et al.* 2021b; Yilmaz *et al.* 2021). Groundwater or a high moisture layer is located between the base rock and pyroclastic flow deposits, which saturation with rainwater may induce the linear sliding of the lava lobes (Hirakawa *et al.* 2018). Subsidence of lava lobes was confirmed by airborne laser scanning between 2004 and 2013 (Shi *et al.* 2018). Recently, the GBSAR was combined with the eXtended RAder Information Network (XRAIN) rainfall radar system to analyse the possible rainfall-induced gravity movement of lava lobes (Dakai *et al.* 2024). All these observations indicate that the stability of the lava lobes decreases over time, and the sliding of the lava lobes is expected in the future. Hirakawa *et al.* (2018) estimated the volume of possibly collapsed rocks and the covered area to be 10^7 m^3 and 7×10^4 m^2, respectively.

The Ministry of Land, Infrastructure, Transport and Tourism (MLIT) and its collaborators are developing an integrated monitoring and early warning system by combining different *in situ* and remote monitoring techniques (Hirakawa *et al.* 2018): prisms are installed on the summit and Total Stations (TS) are installed near the volcano for monitoring of the lava lobes by distance measurements on an hourly basis. The GBSAR is operating 1500 m distant in the southeast direction from the summit and serves data with a periodic time of 7 min; however, monitoring periods are set to 2 d to avoid atmospheric effects. Seismometers and seismic intensity meters are installed on the lava lobes and around the volcanic edifice to detect rockfalls, debris flows and pyroclastic flows. Tilt meters and wire sensors provide data on a daily basis from the top of the lava lobes. Tanaka (2016) measured and differentiated the densities of base rocks (2000 kg m^{-3}) and deposits (400–600 kg m^{-3}) in 3 hr by airborne muography. However, the spatial resolution was limited, and only the peak region was targeted. In this work, we attempted to resolve the internal density structure of Mount Unzen with a higher spatial resolution within a larger volume to clarify a more holistic picture of the lava lobes' structure and evolution.

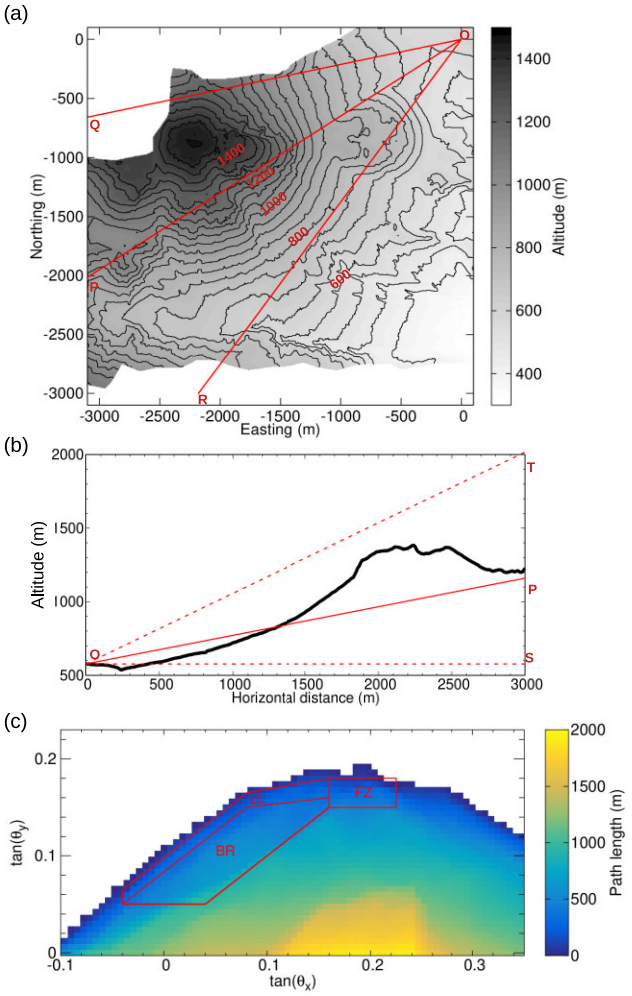

Figure 2. The measurement arrangement at Mount Unzen. (a) The topographic map of the measurement site is shown for an area of 3100 m × 3100 m with a grid size of 5 m × 5 m based on the digital elevation model data of the Ministry of Land, Infrastructure, Transport and Tourism. The observational instrument was installed at (0,0). The OP line shows the azimuthal orientation of the observation instrument that was set to 236.5° from north [defined as $\tan(\theta_x) = 0$]. (b) A cross-section of Mount Unzen along the OP line is shown. The elevation angle acceptance is shown within the OS and OT lines. (c) Path lengths of muons calculated across the volcano from the location of the observation instrument. Lines designate the studied regions across the base rock (BR), the fracture zone (FZ) and the lava lobes (LL).

3. METHODS

3.1 Experimental setting and data collection

We installed a multi-wire proportional chamber (MWPC)-based MOS at a longitude of 130.322515 E° and a latitude of 32.769151 N° at an altitude of 576 m above sea level at a distance of about 2000 m in a northeast direction from the Fugendake peak. The MOS was oriented to the azimuthal direction of 236.5° from north and tilted up 11.5° from the horizontal direction. Fig. 2(a) shows the topographic map of the measurement site around the location of MOS (O) based on the digital elevation model (DEM) of the volcanic field. This DEM was created with a grid size of 5 m × 5 m based on data acquired by laser profiler by the MLIT in December 2022. In Fig. 2(a), black contour lines show the elevations with a stepping of 50 m. The OP line indicates the azimuthal orientation of muographic observation. The OQ and OR lines show the azimuthal open angle of observation. Fig. 2(b) shows a cross-section of Mount Unzen along the OP line of Fig. 2(a). The OS and OT lines bound the elevations from which muons arrived into the MOS. Fig. 2(c) shows the path lengths of muons across Mount Unzen calculated from the measurement site in the coordinate system of MOS (see Section 4.2). The average rock thickness through the BR, FZ and LL regions was quantified from the DEM at 536, 293 and 241 m, respectively.

The MOS has the same structure as the tracking systems applied in Sakurajima Muography Observatory (Oláh *et al.* 2018): as it is

Figure 3. Photograph of the muographic observation instrument that was assembled from six gaseous tracking detectors and five 2-cm-thick lead plates (Oláh *et al.* 2018).

shown in Fig. 3, the tracking system was built up from six MWPC gaseous detectors for muon tracking and five 2-cm-thick lead walls to absorb and deflect low-energy particles (electrons, low-energy muons, etc.) which did not penetrate the volcano but were observed from its directions (Nishiyama *et al.* 2016). Microcomputer-based detector control and data acquisition system was applied. Continuous power and gas supply ensured detector operation during the measurement campaign. The power supply of +12 V direct current was provided with two lithium-ion phosphate batteries. Gas supply was provided with an environmentally friendly gas mixture with Ar and CO_2 gases in a proportion of 80 per cent and 20 per cent, respectively. The data collection was performed for 203 d between 2024 March 28 and December 14. A triple coincidence of MWPCs triggered data collection. The trigger rate was a few Hz. The trigger was blocked for 10^{-4} s during the data readout. The data were acquired into ASCII files on an event-by-event basis. There were two longer technical stops in data collection due to temporary issues with the detector. There were a few shorter technical stops for maintenance work: batteries were replaced every two weeks, and the gas bottle was exchanged two times during the campaign. Remote access to the tracking system was not established. The data were downloaded during the technical stops. Offline data analysis was conducted for performance monitoring and image processing.

3.2 Track reconstruction and flux calculation

An event-by-event track reconstruction procedure was applied independently in the horizontal and the vertical directions (Oláh *et al.* 2018). In the first step, an algorithm determined the continuous sequences of particle hits (clusters) by calculating the positions of centroids, sizes and numbers on an MWPC-by-MWPC basis. In the next step, a combinatorial algorithm based on linear fitting reconstructed the track candidates. The slope [tangents of horizontal (θ_x) and elevation (θ_y) angles], the intercept and the goodness of fit were determined for each track candidate. The track candidates were sorted based on the chi-square per number of degrees of freedom, χ^2/NDF (NDF = 4 for 6 MWPCs), and the best-fitting track candidate was chosen. The tracking efficiency was also quantified for each MWPC by an algorithm that chose a specific detector and reconstructed the trajectory of the particle from all chambers except the investigated one. If there was a straight track, then the algorithm checked the presence of a cluster within a fiducial zone (typically two detector segments) around the extrapolated coordinate in the investigated MWPC. The tracking efficiency was determined by the ratio of the number of cases when there was a cluster to the number of extrapolations. Track reconstruction enabled the quality assurance of the data before the flux calculation. Figs 4(a) and (b) show the variations of the main parameters of detector performance with a time bin size of 3 hr during the data collection period. The frequency of tracks (black error bars) shows variations of below 2.5 per cent during the data collection period, mainly due to atmospheric temperature changes, which affect the production of muons (MINOS Collaboration 2010). The tracking efficiencies were found to be above 95 per cent for each MWPC. The efficiency of tracking on five out of six MWPCs approached 100 per cent.

The tracks were counted as a function of the slopes of the reconstructed tracks. The muon flux (F) was calculated for each $\Delta\tan(\theta_x)$–$\Delta\tan(\theta_y)$ bin by dividing the number of straight (χ^2/NDF < 1.25 in both directions) tracks (N) with sensitive surface area, the covered solid angle and the duration of data acquisition. The slope size was chosen to be 0.006×0.006 for this study.

Fig. 4(c) shows the distribution of χ^2/NDF. The χ^2/NDF cut of 1.25 was set to exclude the sub-GeV background muons. Fig. 4(d) shows the track counts in $\Delta\tan(\theta_x)$–$\Delta\tan(\theta_y)$ angular bins for the region of interest. The corresponding flux and flux error maps are respectively shown in Figs 4(e) and (f). The track and flux maps reflect the shape of Mount Unzen (e.g. visualize the spine on the summit) and indicate the inverse relation between the muon yield and rock thickness.

3.3 Correction of atmospheric temperature effects

Most systematic effects of muon flux measurements are negligible (Lesparre *et al.* 2010). The changes in the atmosphere's thermal state affect the production of muons and thus the muon flux (MINOS Collaboration 2010; Tramontini *et al.* 2019). The relative change of muon flux (ΔF/F) was calculated by the following formula:

$$\Delta F/F = \alpha_T \times \Delta T_{eff}/T_{eff}, \quad (1)$$

where α_T is the temperature coefficient and T_{eff} is the effective temperature that is the weighted average of temperatures measured at different altitudes. The $\alpha_T \approx 1$ was estimated from this experiment. The effective temperature was calculated using the procedure developed for the MINOS experiment (MINOS Collaboration 2010) and the atmospheric weather data that were collected at the nearest meteorology station with the identification number of 47 807 (University of Wyoming 2021). The zenith angle and energy threshold were set to 70 GeV and 71°, respectively. Fig. 5 shows the changes in effective temperature throughout the measurement period. The average value was estimated at 230.2 °K. The effective temperature values varied within ± 3 per cent around the average value. The effective temperatures were averaged for each time bin, and the relative flux was corrected according to the above formula.

3.4 Forward modelling of muon flux for density calculation

Muography reconstructs the average density-length (density integrated along the path of muons, X) through the volcano for each angular bin:

$$X = L \times \rho, \quad (2)$$

where L is the path length of muons through the volcano (Fig. 2c), the ρ is the average density of volcanic materials. The relatively

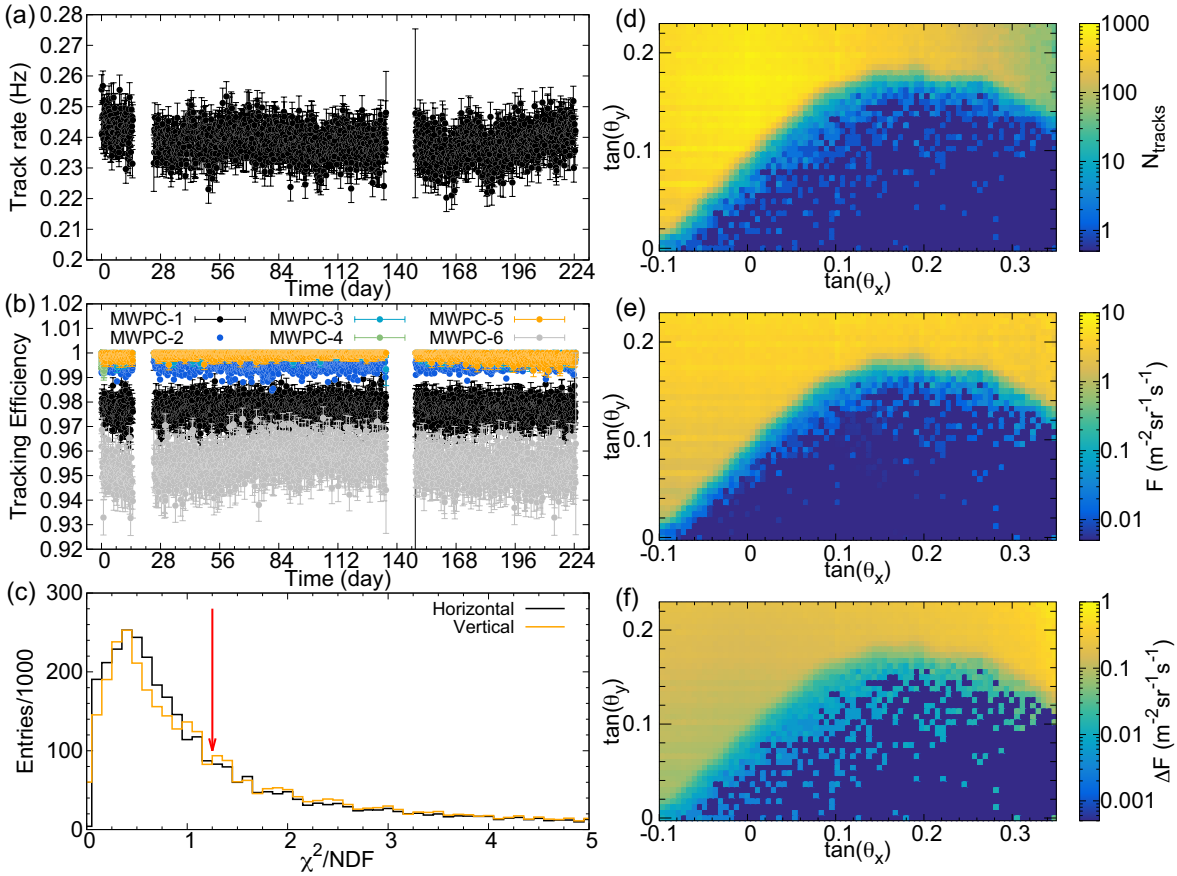

Figure 4. Results of track reconstruction and muon flux calculation. (a) Track rate is shown with a time binning of 3 hr for the data collection period. (b) Track detection efficiencies of the six detector layers of the observation instrument are shown with a time binning of 3 hr for the data collection period. (c) The distribution of the chi-square per number of degrees of freedom for the reconstructed tracks. The arrow shows the track selection cut of $\chi^2/\mathrm{NDF} < 1.25$ applied for this work. (d)–(f) The track counts, muon flux and flux error are respectively shown in an angular binning that is based on the horizontal and vertical slopes of reconstructed tracks. Each angular bin has a size of $\Delta\tan(\theta x) \times \Delta\tan(\theta y) = 0.006 \times 0.006$.

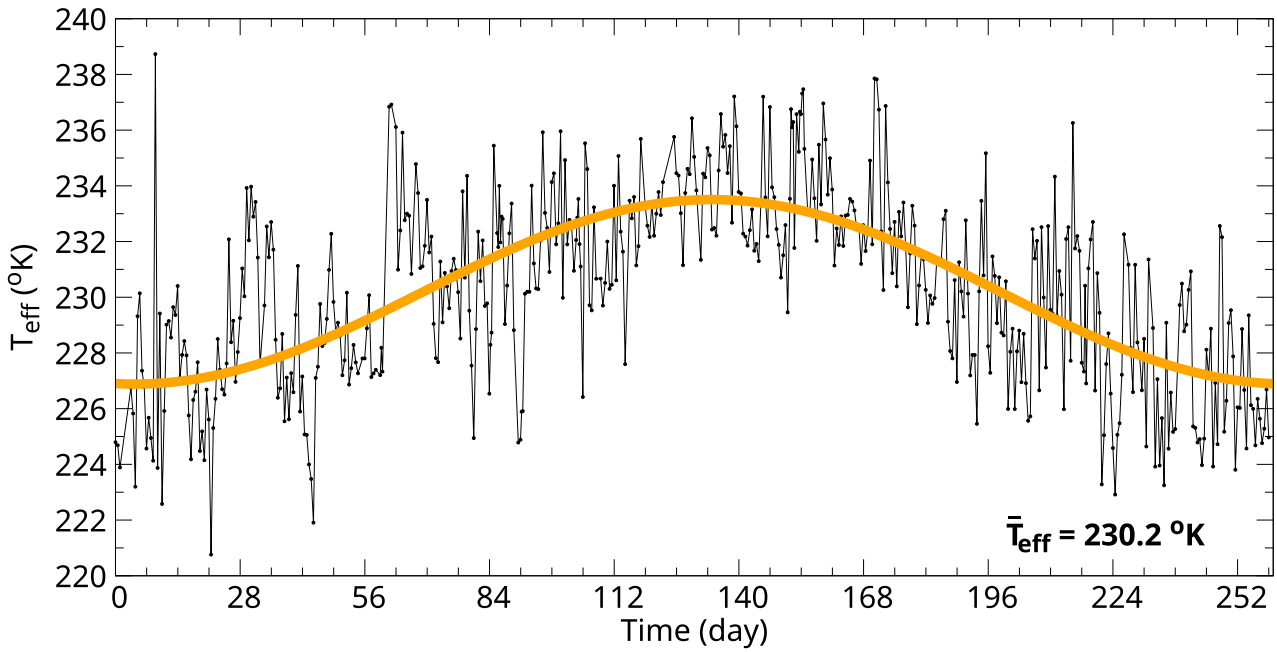

Figure 5. The time-line of effective temperatures is shown for the entire data collection period. The cosine fit shows an average seasonal variation of 6 °K around the average value of 230.2 °K.

short time period from production and sufficient spatial resolution of DEM data allowed us to calculate path lengths accurately. We reconstructed the density for each angular bin with the following procedure. First, the density-lengths were reconstructed via comparing the measured fluxes to modelled fluxes. The measured flux error was respectively added and subtracted to determine the lower and upper errors of density-lengths via the same procedure. The modelled fluxes were determined by integrating the zenith angle and energy-dependent flux of muons from minimum energies required for the muons to penetrate across the volcano:

$$F = \int_{\mathrm{Emin}} \mathrm{f}(\mathrm{E}, \theta)\, \mathrm{dE}. \tag{3}$$

The minimum energies were determined using the data tables calculated by the continuous slowing down approximation (Groom *et al.* 2002). Here, we applied a parametrization of a modified-Gaisser model (Tang *et al.* 2006). The altitude dependence of muon spectra was taken into account:

$$\mathrm{F}(\mathrm{H}) = \mathrm{F}(0) \times \mathrm{e}^{-\mathrm{H}/\mathrm{L}(\mathrm{E})}, \tag{4}$$

where

$$\mathrm{L}(\mathrm{E}) = 4900 + 750 \times \mathrm{E}. \tag{5}$$

We note that the applied flux model underestimated the flux below up to a few GeVs because it was parametrized using fluxes measured at higher energies. Consequently, our procedure overestimated the densities for thicknesses below a few tens of metres.

4. RESULTS

4.1 First high-definition density image of Mount Unzen

Figs 6(a) and (b) show the muographic density images of Mount Unzen with the slope bin size of 0.006 × 0.006. This slope binning resolves the density structure of the volcanic edifice with a spatial resolution of 12 m × 12 m from a distance of 2000 m. The white-shaded regions correspond to slope bins without densities due to the thickness that was not penetrated by muons during the data collection period. The BR, the FZ and the LL are shown within the red-coloured lines. The ground deformation is negligible relative to the spatial resolution of the muographic imaging for the designated volcanic regions. Figs 6(c)–(e) show the distributions of density values extracted from the selected regions. The densities ranged from 1000 to 4750 kg m^{-3} with a mean of 2470 kg m^{-3} for the volcano's base rock (Fig. 6c). The density values were measured between 500 and 4750 kg m^{-3} with a mean of 2290 kg m^{-3} for the fracture zone (Fig. 6d). For the lava lobes (Fig. 6e), the density ranged from 500 to 4000 kg m^{-3} with a mean of 1570 kg m^{-3}.

4.2 Density-length monitoring across Mount Unzen

The finite yield of cosmic-ray muons and its attenuation in the volcanic rocks result in constraints on the observation duration and the muon detector acceptance. Calculation of these observational parameters is required for the design and optimization of the experiment. The time required to resolve a density-length variation across the lava lobes should not exceed the period of causative phenomena, either density-length decrease due to rock falls or density-length increase by groundwater saturation due to heavy rainfalls. The measurement time Δt required to measure a density-length contrast of $\pm\Delta X$ with a detector acceptance of A with SD standard deviations is estimated as follows.

$$\Delta t > \mathrm{F}(\mathrm{X}) / [\mathrm{F}(\mathrm{X}) - \mathrm{F}(\mathrm{X} \pm \Delta \mathrm{X})]^2 \times [1/\mathrm{A}] \times \mathrm{SD}^2, \tag{6}$$

where F(X) and F(X±ΔX) are the muon fluxes calculated after X and (X±ΔX) density-lengths, respectively. Therefore, the measurement time is inversely proportional to the detector acceptance and proportional to the square of standard deviations. To determine the time sequence of muon monitoring, we calculated the measurement times as a function of density-length variation. Fig. 7 shows the estimated measurement times required to measure given density-length increases (solid lines) and decreases (dashed lines) across the BR (blue-coloured lines), the FZ (green-coloured lines) and the LL (orange-coloured lines) with 1 standard deviation with the current detector acceptances of 2.89×10^{-3}, 2.36×10^{-4}, 1.02×10^{-3} m^{-2} sr^{-1}, respectively. We set the time periods to 7 d to observe 2–3 standard deviation density-length variations across the lava lobes within these periods.

Fig. 8(a) shows the time evolution of the difference between the average (arithmetic mean values) of density-lengths with one standard deviation error bars measured for the BR (blue-coloured error bars) and FZ (green-coloured error bars) regions for 7-d periods and the average density-lengths determined for the entire period. The density-lengths did not change significantly around the average value for the regions BR, FZ during the data collection period. An exception is the end of June when density-length increased across the BR after heavy rains occurred between day 84 and day 105. Fig. 8(b) shows the same quantities for the lava lobes (LL, orange-coloured error bars). Daily precipitation versus time was also calculated from the data of hourly precipitation measured by the Japan Meteorological Agency (2025). The daily precipitation is shown with turquoise-coloured histograms in Figs 8(a) and (b). The density-lengths did not increase across the LL region, except in the middle of May (days 42–48) and from the end of June to the beginning of July (days 84–105), when a relatively large amount of rain fell with two precipitation peaks of above 240 mm per day.

5. DISCUSSION

5.1 Long-term weakening of lava lobes inferred from density reduction

Figs 6(a)–(c) show that the mean density of the lava lobes (1570 kg m^{-3}) is significantly lower than the mean densities of the base rock (2470 kg m^{-3}) and the fracture zone (2290 kg m^{-3}). The muographically measured base rock density closely matches the range of 2 500–2600 kg m^{-3} that were quantified from log data collected by the USDP (Ikeda *et al.* 2008). The slight difference is caused by the lava lobes which are covering the base rock (Fig. 1). The mean density of the fracture zone is also consistent with values between 1 900 to 2400 kg m^{-3} with a mean of 2200 kg m^{-3} that were measured by a portable device based on the Archimedean principle at the summit of the volcanic edifice (Kueppers *et al.* 2005). The smaller density of the fracture zone relative to the base rock is explained by higher porosity of dyke samples that were fractured during magma transport, emplacement and cooling, as well as hydrothermal alteration (Yilmaz *et al.* 2021). The muographically measured density of the lava lobes was significantly lower than their density during the eruption of 1990–1995, which increased from 2000 to 2500 kg m^{-3} due to decreasing vesicularity of new lava flows (Nakada *et al.* 1999). It is worth noting that Tanaka (2016) also reported density

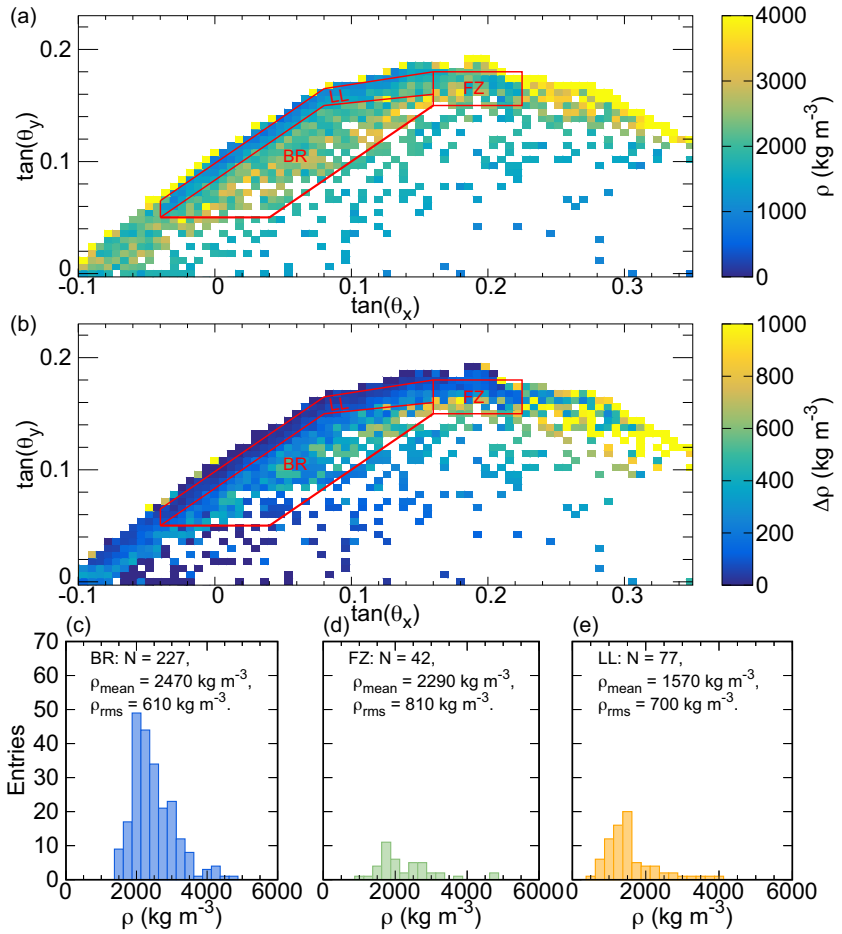

Figure 6. First high-definition muography of Mount Unzen. (a)–(b) The measured density and density errors are shown with a slope size of $\Delta\tan(\theta x) \times \Delta\tan(\theta y) = 0.006 \times 0.006$. The white-shaded regions correspond to slope bins without density values due to the thickness that was not penetrated by muons. (c)–(e) Distributions of density values extracted from base rock (BR), fracture zone (FZ) and lava lobes (LL) regions (Figs 6a and b) are shown.

contrast between the base rock and the lava dome, but with significantly lower absolute values of 2000 kg m^{-3} for the base rock and 700 kg m^{-3} for the lava lobes. However, those muographic snapshots had significantly coarser spatial resolution of 90 m to minimize the data collection time and the densities were under-measured due to the detection of more particles which did not penetrate across the edifice. Similarly to our work, Carbone *et al.* (2013) observed a strong density contrast between the bulk rock of the volcanic edifice and a mechanically weakness zone corresponding to a pit crater on the eastern flank of the Southeastern Crater of Mount Etna, Italy. Rosas-Carbajal *et al.* (2017) conducted joint analysis of muography and gravimetry data and found a low-density, mechanically weak region in the southern part of La Soufrière de Guadeloupe lava dome in the eastern Caribbean where the hydrothermal system was active. The density reduction observed in the lava lobes of Mount Unzen suggests a similar structural weakening over time since the last eruption, in accordance with the previous observations using gravimetry (Saibi *et al.* 2010), airborne laser scanner (Shi *et al.* 2018) and radar (Daikai *et al.* 2024). Similarly to the reduction of rock strength in the La Soufrière de Guadeloupe lava dome (Heap *et al.* 2021b, 2022), the progressive weakening of the lava lobes of Mount Unzen likely occurred due to the alteration of rocks. Here the alteration was induced by the subsurface hydrothermal circulation in the shallow plumbing system and the groundwater flows from the summit region towards lower elevations (Hashimoto & Tanaka 1995; Saibi *et al.* 2010). Figs 8(a) and (b) indicate that density-length values did not change significantly across the different volcanic regions during the data collection period. Therefore, the timeline of density-lengths from 2024 March 28 to December 12 does not indicate any additional weakening of the three designated zones. This observational result implies that the rocks are completely hydrothermally altered or hydrothermal alteration requires longer timescales. Yilmaz *et al.* (2021) found that the rocks completely altered in the conduit zone (FZ in this study) by fluid flows occurred within 9 yr after the eruption 1990–1995. Long-term (multi-year) muographic monitoring would allow to detect progressive weakening of the lava lobes and a better understanding of the underlying processes.

5.2 Muon monitoring of heavy rainfall induced mass gains in the lava lobes

Besides structural weakening, heavy rainfall can result in short-term mass gains that induce gravitational destabilization of lava lobes (Daikai *et al.* 2024). When a large volume of water flows over or gravitationally infiltrates into lava lobes, the average density-length of the lobes increases; thus, muography is expected to detect changes in density-lengths. The applicability of muon monitoring of groundwater has already been demonstrated in a mechanically fractured fault zone (Tanaka *et al.* 2011), a groundwater table (Tanaka &

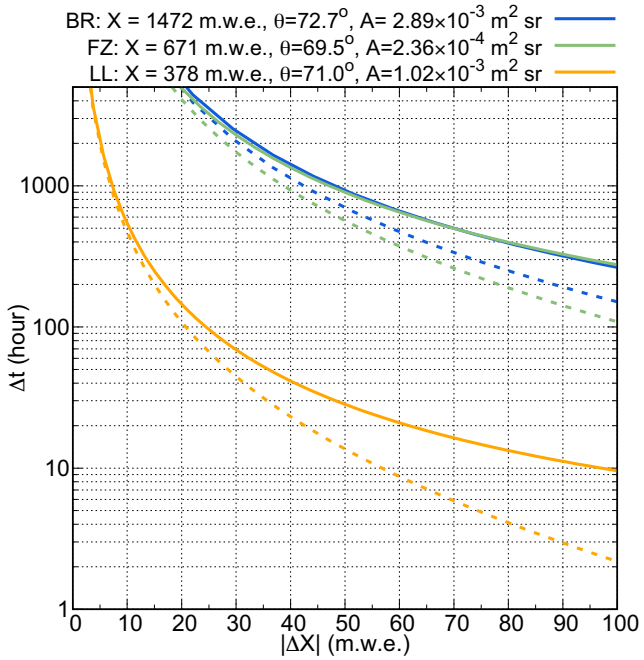

Figure 7. The measurement times calculated to observe ΔX density-length increase (solid lines) and decrease (dashed lines) with 1 standard deviation uncertainty with the muon detector acceptances that covered the base rock (BR, blue-coloured lines), the fracture zone (FZ, green-coloured lines) and the lava lobes (LL, orange-coloured lines), respectively.

Sannomiya 2013) and a karstified aquifer (Tramontini *et al.* 2024). Moreover, combining measurements of muon and the electromagnetic components of cosmic rays has achieved an improved sensitivity to groundwater (Taketa *et al.* 2022). The density-length increase across the BR in late June (Fig. 8a) is interpreted as the effect of water accumulated in the lava lobes covering the base rock (Fig. 1). In contrary, fractures and hydrothermally altered minerals could hold the water in the zone FZ, we did not observe significant increase of density-length (Fig. 8a). The water may flow from FZ toward lower elevations (Hashimoto & Tanaka 1995; Saibi et al. 2010). Fig. 8(b) shows that the density-lengths increased across the lava lobes by about 20 m-water-equivalent (m.w.e.) during and after heavy (>240 mm per day) rainfall events. This is consistent with ground-based radar observations indicating surface deformation of the lava lobes during earlier rainy periods (Daikai *et al.* 2024). The amount of rainfall that triggered density-length changes is comparable to previous events (>150 mm accumulated over 2 d and several episodes of <100 mm per 2 d) that induced lava lobe surface deformation (Daikai *et al.* 2024). The first significant density-length change occurred within a period of 7 d. This duration is similar to the post-eruptive lava dome collapse timescales that occurred on Soufrière Hills Volcano, Montserrat (Calder *et al.* 2002). The second density-length change was observed after day 84, and lasted approximately 3 weeks. This duration is consistent with the duration of surface deformation reported by Daikai et al. (2024). When the density-lengths reached their local maxima, those started to decrease within a few days because highly fractured rocks are highly permeable for water. Therefore, the short-term density-length increases had no impact on the stability of the lava lobes during the measurement period.

5.3 Prospects of muography as a new complementary tool for lava dome monitoring

Fig. 6 indicates that high-definition muographic imaging can complement rock sampling in volcanic regions that are hardly accessible due to the complex topography or ongoing volcanic crisis. Moreover, dynamic 3-D muon imaging would allow us to explore the internal structure of the lava dome with full spatial coverage (Rosas-Carbajal *et al.* 2017), build rock strength distribution and alteration maps (Heap *et al.* 2021b; Poganj *et al.* 2025), and monitoring those. A joint analysis of the time-series of muographic and ground surface deformation data would aid some limitations of deformation monitoring techniques (Oláh *et al.* 2023). For example, muography could support GBSAR and airborne radar techniques in situations where those are not sensitive to mass wasting or gaining phenomena that occurred without associated ground deformations, or when their signals are disrupted temporarily by volcanic ash in the atmosphere or dense vegetation on the volcano's flank.

An immediate (up to a few minutes) early warning is required at the residential area near Mount Unzen, as a debris avalanche triggered by a large collapse of lava lobes could reach the area in approximately 5 min (Hirakawa *et al.* 2018). The volume of collapsed material is estimated to be about 10^7 m^3, representing less than 5 per cent of the total lava lobe volume of 2.1 × 10^8 m^3. Assuming uniform rock density, this corresponds to an average density-length reduction of about 5 per cent, about -19 m.w.e. across the 378 metre-water-equivalent-thick LL region. Based on the dashed orange-coloured line of Fig. 7, measuring a -19 m.w.e density-length reduction across the LL with at least 2 standard deviations within 5 min would require a muon monitoring system with an acceptance of 5.43 m^{-2} sr^{-1}. The current development level of detector technologies and their costs do not allow us to construct and operate such a large acceptance observatory; thus, it is not possible to monitor the density-length changes across the entire lava lobes and provide warnings within a few minutes. A more realistic approach to monitor rockfalls from the upper shallow part of the lava lobes, where the removal of just a few metres of materials can lead to about an order-of-magnitude flux increase as shown in Figs 4(d) and (e) between the open air and the volcano's ridge. As it is indicated in Figs 3(d), (e), (f), 6(a) and (b), muography can achieve the desired spatial resolution of a few metres. The muographic monitoring of rockfalls will be tested in future works (e.g. Truffert *et al.* 2023). Concerning short-term (from a few hours to a few days) and intermediate-term (from a few days to a few months) assessment of post-eruptive hazards, Fig. 8(b) suggests that it will be possible to monitor the saturation of groundwater in the lava lobes due to heavy rainfalls and groundwater inflows induced by hydrothermal processes with the upgrade of the current setup. The MWPC technology has already been applied in a modular observation system, and its long-term (more than eight years) operation has been verified in the Sakurajima Muography Observatory (Oláh *et al.* 2021). An observatory of a similar size would allow us to monitor the density-length changes due to groundwater saturation across the flank and support the stability analysis on a daily basis.

6. CONCLUSIONS

We have shown that muography is applicable for resolving the internal density structure of lava lobes with an unprecedented spatial resolution of a few metres. Muographic imaging enables the localization of structurally weak zones and can support targeted rock sampling. Monitoring of density-lengths via muography provides

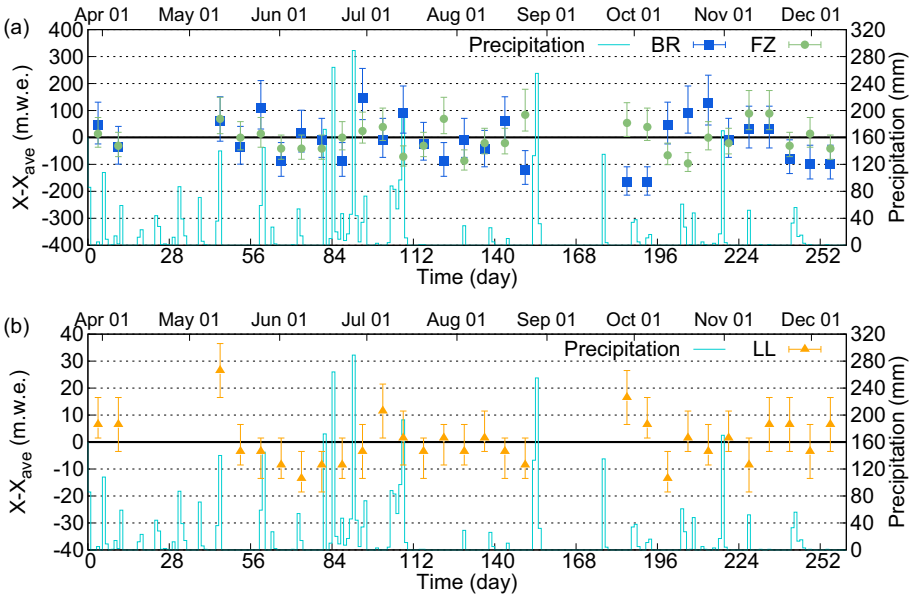

Figure 8. The timelines of density-length changes across the designated volcano regions relative to the average density-lengths measured for the entire period are shown with 1 standard deviation error bars and with a time binning of 7 d. (a) The density-length variation versus time is shown for the base rock (BR, filled rectangles with error bars) and the fracture zone (FZ, filled circles with error bars). (b) The density-length variation is shown as a function of time for the lava lobes (LL, filled triangles with error bars). Histograms show the daily precipitation data in both panels.

complementary data for lava dome surveillance. Our observations indicate that the lava lobes remained stable during the data collection period, with no evidence of structural weakening. However, short-term density-length changes were detected within the lava lobes, likely caused by heavy rainfall events. Real-time muographic monitoring will provide useful complementary information as a part of an integrated early warning system for short-term and long-term volcano stability assessment by expansion of muographic observation system and implementation of automated data processing system.

ACKNOWLEDGMENTS

This work was supported by the Ministry of Land, Infrastructure, Transport and Tourism, Japan, and the Sabo Frontier Foundation. LO, DV and TL are supported by the Hungarian NKFIH research grant under identification number TKP2021-NKTA-10, the HUN-REN Welcome Home and Foreign Researcher Recruitment Programme KSZF-144/2023. Detector construction and testing were completed within the Vesztergombi Laboratory for High Energy Physics (VLAB) at HUN-REN Wigner RCP. We thank to Toshio Mori, Yukihiko Sakatani and Ryo Ogasawara for the technical support provided to this project.

DATA AVAILABILITY

The data underlying this paper are available in OSF data repository, at https://doi.org/10.17605/OSF.IO/FJ5GS.

REFERENCES

Athanassas, C.D., 2020. Muography for geological hazard assessment in the South Aegean active volcanic arc (SAAVA), *Mediterr. Geosci. Rev.,* **2,** 233–246

Balázs, L., Nyitrai, G., Surányi, G., Hamar, G., Barnaföldi, G.G. & Varga, D., 2024. 3-D muographic inversion in the exploration of cavities and low-density fractured zones, *Geophys. J. Int.,* **236,** 700–710

Beni, T. *et al.* 2025. Use of muon imaging for enhanced reconstruction of underground cavities and associated stability conditions at a historical mining site, *Eng. Geol.,* **353,** 108141

Biggs, J., Ebmeier, S.K., Aspinall, W.P., Lu, Z., Pritchard, M.E., Sparks, R.S.J. & Mather, T.A., 2014. Global link between deformation and volcanic eruption quantified by satellite imagery, *Nat. Commun.,* **5,** 3471

Byrdina, S. *et al.* 2017. Geophysical image of the hydrothermal system of Merapi volcano, *J. Volc. Geoth. Res.* **319,** 30–40

Calder, E.S., Luckett, R., Sparks, R.S.J. & Voight, B., 2002. Mechanisms of lava dome instability and generation of rockfalls and pyroclastic flows at Soufrière Hills Volcano, Montserrat, *Geol. Soc. Lond. Mem.,* **21,** 173–190

Carbone, D., Gibert, D., Marteau, J., Diament, M., Zuccarello, L. & Galichet, E., 2013. An experiment of muon radiography at Mt. Etna (Italy), *Geophys. J. Int.,* **196,** 633–643

Daikai, R., Gomez, C., Hotta, N. & Shinohara, Y., 2024. Rainfall-induced gravity movement of the Unzen-Fugendake volcanic dome analysis combining ground-radar interferometry and XRAIN Rainfall radar system, *IOP Conf. Ser. Earth Environ. Sci.,* **1313,** 012026

Darmawan, H. *et al.* 2022. Hidden mechanical weaknesses within lava domes provided by buried high-porosity hydrothermal alteration zones, *Sci. Rep.* **12,** 3202

Darmawan, H., Walter, T.R., Troll, V.R. & Budi-Santoso, A., 2018. Structural weakening of the Merapi dome identified by drone photogrammetry after the 2010 eruption, *Nat. Hazard,* **18,** 3267–3281

Dumont, Q., Cayol, V., Froger, J.-L. & Peltier, A., 2022. 22 years of satellite imagery reveal a major destabilization structure at Piton de la Fournaise, *Nat. Commun.,* **13,** 2649

Elsworth, D. & Voight, B., 2001. The mechanics of harmonic gas pressurization and failure of lava domes, *Geophys. J. Int.,* **145,** 187–198

Gibert, D. *et al.* 2022. Observation of the dynamics of hydrothermal activity in La Soufrière of Guadeloupe volcano with joint muography, gravimetry, electrical resistivity tomography, seismic and temperature monitoring, *Geophys. Mon. Ser.* **270,** 55–73

Giudicepietro, F. *et al.* 2023. Seismic and thermal precursors of crater collapses and overflows at Stromboli volcano, *Sci. Rep.* **13,** 11115

Groom, D.E., Mokhov, N.V. & Striganov, S.I., 2002. Muon stopping power and range tables 10 MeV-100 TeV, *At. Data Nucl. Data Tables,* **76,** 183–356.

Hashimoto, T. & Tanaka, Y., 1995. A large self-potential anomaly on Unzen Volcano, Shimabara Peninsula, Kyushu Island, Japan, *Geophys. Res. Lett.,* **22,** 191–194

Heap, M.J. *et al.* 2021a. Hydrothermal alteration can result in pore pressurization and volcano instability, *Geology,* **49 (** 11**),** 1348–1352

Heap, M.J. *et al.* 2021b. Alteration-induced volcano instability at la Soufrière de Guadeloupe (eastern Caribbean), *J. geophys. Res. Solid Earth,* **126 (** 8**),** e2021JB022514

Heap, M.J. *et al.* 2022. The tensile strength of hydrothermally altered volcanic rocks, *J. Volc. Geotherm. Res.,* **428,** 107576

Heap, M.J. & Violay, M.E.S., 2021. The mechanical behaviour and failure modes of volcanic rocks: a review, *Bull. Volcanol.,* **83,** 33

Hirakawa, Y., Usuki, N., Fujita, K., Tanaka, T., Kaneko, M., Ueno, T., Eguchi, H. & Shimokubo, K., 2018. Monitoring system of a large rockslide in Heisei-Shinzan Lava Dome, Mt. Unzen, Japan, in *Symp. Proc. of the INTERPRAENENT 2018 in the Pacific Rim,* **2018,**pp. 1–10. Available at: https://archive.interpraevent.at/palm-cms/upload_files/Publikationen/Tagungsbeitraege/2018_1_363.pdf

Holma, M., Zhang, Z., Kuusiniemi, P., Loo, K. & Enqvist, T., 2022. Future prospects of muography for geological research and geotechnical and mining engineering, *Geophys. Mon. Ser.,* **270,** 199–219

Hornby, A.J. *et al.* 2015. Spine growth and seismogenic faulting at Mt. Unzen. Japan, *J. geophys. Res. Solid Earth* **120,** 4034–4054

Ikeda, R., Kajiwara, T., Omura, K. & Hickman, S., 2008. Physical rock properties in and around a conduit zone by well-logging in the Unzen, Scientific Drilling Project, Japan, *J. Volc. Geotherm. Res.,* **175,** 13–19.

Japan Meteorological Agency, 2025. https://www.data.jma.go.jp/risk/obsdl/index.php

Kueppers, U., Scheu, B., Spieler, O. & Dingwell, D.B., 2005. Field-based density measurements as tool to identify preeruption dome structure: set-up and first results from Unzen volcano, Japan, *J. Volc. Geotherm. Res.,* **141,** 65–75

Lechmann, A. *et al.* 2018. The effect of rock composition on muon tomography measurements, *Solid Earth,* **9,** 1517–1533

Lechmann, A. *et al.* 2021. Muon tomography in geoscientific research—A guide to best practice, *Earth-Sci. Rev.,* **222,** 103842

Lesparre, N., Gibert, D., Marteau, J., Déclais, Y., Carbone, D. & Galichet, E., 2010. Geophysical muon imaging: feasibility and limits, *Geophys. J. Int.,* **183,** 1348–1361

Liu, G. *et al.* 2024. Deep investigation of muography in discovering geological structures in mineral exploration: a case study of Zaozigou gold mine, *Geophys. J. Int.,* **237,** 588–603

López, D.L. & Williams, S.N., 1993. Catastrophic volcanic collapse: relation to hydrothermal processes, *Science,* **260,** 1794–1796

Lo Presti, D. *et al.* 2020. Muographic monitoring of the volcano-tectonic evolution of Mount Etna, *Sci. Rep.* **10,** 11351

Macedonio, G. *et al.* 2022. Muography of the volcanic structure of the summit of Vesuvius, *Geophys. Mon. Ser.,* **270,** 123–136.

Matsushima, J. *et al.* 2024. Joint measurement of cosmic-ray muons and seismic waves at laboratory scale, *Geophys. J. Int.,* **239,** 1821–1832

McGuire, W., Pullen, A. & Saunders, S., 1990. Recent dyke-induced large-scale block movement at Mount Etna and potential slope failure, *Nature,* **343,** 357–359

MINOS Collaboration, 2010. Observation of muon intensity variations by season with the MINOS far detector, *Phys. Rev. D,* **81,** 012001

Miyamoto, S. *et al.* 2010. Muography of 1949 fault in La Palma, Canary Islands, Spain, *Ann. Geophys.,* **60,** S0110.

Müller, D., Bredemeyer, S., Zorn, E., De Paolo, E. & Walter, T.R., 2021. Surveying fumarole sites and hydrothermal alteration by unoccupied aircraft systems (UAS) at the La Fossa cone, Vulcano Island (Italy), *J. Volc.. Geotherm. Res.,* **413,** 107208.

Nagahara, S., Miyamoto, S., Morishima, K., Nakano, T., Koyama, M. & Suzuki, Y., 2022. Three-dimensional density tomography determined from multi-directional muography of the Omuroyama scoria cone, Higashi-Izu monogenetic volcano field, Japan, *Bull. Volcanol.,* **84,** 94

Nakada, S., Shimizu, H. & Ohta, K., 1999. Overview of the 1990-1995 eruption at Unzen Volcano, *J. Volc. Geotherm. Res.,* **89,** 1–22

Nakada, S., Uto, K., Sakuma, S., Eichelberger, J.C. & Shimizu, H., 2005. Scientific results of conduit Drilling in the Unzen Scientific Drilling Project (USDP), *Sci. Dril.,* **1,** 18–22

Nishiyama, R., Miyamoto, S., Okubo, S., Oshima, H. & Maekawa, T., 2017. 3D density modeling with gravity and muon-radiographic observations in Showa-Shinzan Lava Dome, Usu, Japan, *Pure appl. Geophys.,* **174,** 1061–1070.

Nishiyama, R., Taketa, A., Miyamoto, S. & Kasahara, K., 2016. Monte Carlo simulation for background study of geophysical inspection with cosmic-ray muons, *Geophys. J. Int.,* **206,** 1039–1050

Oláh, L. *et al.* 2023. Muon imaging of volcanic conduit explains link between eruption frequency and ground deformation, *Geophys. Res. Lett.* **50,** e2022GL101170

Oláh, L., Tanaka, H.K.M. & Hamar, G., 2021. Muographic monitoring of hydrogeomorphic changes induced by post-eruptive lahars and erosion of Sakurajima volcano, *Sci. Rep.,* **11,** 17729

Oláh, L., Tanaka, H.K.M., Ohminato, T. & Varga, D., 2018. High-definition and low-noise muography of the Sakurajima volcano with gaseous tracking detectors, *Sci. Rep.,* **8,** 3207.

Oppenheimer, C., Rothery, D.A. & Francis, P.W., 1993. Thermal distributions at fumarole fields: implications for infrared remote sensing of active volcanoes, *J. Volc. Geotherm. Res.,* **55,** 97–115

Pallister, J., Wessels, R., Griswold, J., McCausland, W., Kartadinata, N., Gunawan, H., Budianto, A. & Primulyana, S., 2019. Monitoring, forecasting collapse events, and mapping pyroclastic deposits at Sinabung volcano with satellite imagery, *J. Volc. Geotherm. Res.,* **382,** 149–163

Peruzzetto, M., Komorowski, J.-C., Le Friant, A., Rosas-Carbajal, M., Mangeney, A. & Legendre, Y., 2019. Modeling of partial dome collapse of La Soufrière de Guadeloupe volcano: implications for hazard assessment and monitoring, *Sci. Rep.,* **9,** 13105

Poganj, A., Heap, M.J. & Baud, P., 2025. Spatial distribution of alteration and strength in a lava dome: implications for large-scale volcano stability modelling, *J. Volc. Geotherm. Res.,* **463,** 108344.

Portal, A. *et al.* 2013. Inner structure of the Puy de Dôme volcano: cross-comparison of geophysical models (ERT, gravimetry, muon imaging), *Geosci. Instrum. Meth. Data Syst.,* **2,** 47–54

Puglisi, G., Bonaforte, A., Ferretti, A., Guglielmino, F., Palano, M. & Prati, C., 2008. Dynamics of Mount Etna before, during, and after the July-August 2001 eruption inferred from GPS and differential synthetic aperture radar interferometry data, *J. geophys. Res. Solid Earth,* **113,** 1–20

Reid, M.E., 2004. Massive collapse of volcano edifices triggered by hydrothermal pressurization, *Geology,* **32**(5), 373–376

Rosas-Carbajal, M., Jourde, K., Marteau, J., Deroussi, S., Komorowski, J.-C. & Gibert, D., 2017. Three-dimensional density structure of La Soufrière de Guadeloupe lava dome from simultaneous muon radiographies and gravity data, *Geophys. Res. Lett.,* **44,** 6743–6751

Rosas-Carbajal, M., Komorowski, J.-C., Nicollin, F. & Gibert, D., 2016. Volcano electrical tomography unveils edifice collapse hazard linked to hydrothermal system structure and dynamics, *Sci. Rep.,* **6,** 29899

Saibi, H., Gottsmann, J. & Ehara, S., 2010. Post-eruptive gravity changes from 1999 to 2004 at Unzen volcano (Japan): a window into shallow aquifer and hydrothermal dynamics, *J. Volc. Geotherm. Res.,* **191,** 137–147

Sato, H., Fujii, T. & Nakada, S., 1992. Crumbling of dacite dome lava and generation of pyroclastic flows at Unzen volcano, *Nature,* **360,** 664–666

Schaefer, L.N., Di Traglia, F., Chaussard, E., Lu, Z., Nolesini, T. & Casagli, N., 2019. Monitoring volcano slope instability with Synthetic Aperture Radar: a review and new data from Pacaya (Guatemala) and Stromboli (Italy) volcanoes, *Earth-Sci. Rev.,* **192,** 236–257

Schouten, D., 2019. Muon Geotomography: selected case studies, *Phil. Trans. R. Soc. A.,* **377,** 20180061

Shi, X., Jiang, Y. & Hirakawa, Y., 2018. Growth and potential collapse of the lava dome in Unzen volcano and the estimation on block-and-ash flows, *Geosci. J.,* **22,** 273–286http://dx.doi.org/10.1007/s12303-017-0051-3

Siebert, L., Glicken, H. & Ui, T., 1987. Volcanic hazards from Bezymianny- and Bandai-type eruptions, *Bull. Volcanol.,* **49,** 435–459

Taketa, A., Nishiyama, R., Yamamoto, K. & Iguchi, M., 2022. Radiography using cosmic-ray electromagnetic showers and its application in hydrology, *Sci. Rep.,* **12,** 20395

Tanaka, H.K.M., 2016. Instant snapshot of the internal structure of Unzen lava dome, Japan with airborne muography, *Sci. Rep.,* **6,** 39741

Tanaka, H.K.M., 2019. Japanese volcanoes visualized with muography, *Phil. Trans. R. Soc. A,* **377,** 20180142

Tanaka, H.K.M. *et al.*, 2023. Muography, *Nat. Rev. Methods Primers,* **3,** 88

Tanaka, H.K.M., Miyajima, H., Kusagaya, T., Taketa, A., Uchida, T. & Tanaka, M., 2011. Cosmic muon imaging of hidden seismic fault zones: rainwater permeation into the mechanical fractured zones in Itoigawa-Shizuoka Tectonic Line, Japan, *Earth planet. Sci. Lett.,* **306,** 156–162

Tanaka, H.K.M. & Sannomiya, A., 2013. Development and operation of a muon detection system under extremely high humidity environment for monitoring underground water table, *Geosci. Instrum. Meth. Data Syst.,* **2,** 29–34

Tang, A., Horton-Smith, G., Kudryavtsev, V.A. & Tonazzo, A., 2006. Muon simulations for Super-Kamiokande, KamLAND, and CHOOZ, *Phys. Rev. D,* **74,** 053007

Tramontini, M., Rosas-Carbajal, M., Nussbaum, C., Gibert, D. & Marteau, J., 2019. Middle-atmosphere dynamics observed with a portable muon detector, *Earth Space Sci.,* **6,** 1865–1876

Tramontini, M., Rosas-Carbajal, M., Zyserman, F.I., Longuevergne, L., Nussbaum, C. & Marteau, J., 2024. Defining the sensitivity of cosmic ray muons to groundwater storage changes, *C. R. Géosci,* **356,** 177–194

Truffert, C., Bouteille, S., Le Moigne, B., Marteau, J., Hueber, N. & Samyn, K., 2023. First results of muon tomography of a giant cliff—The Maido rampart, in *International Meeting for Applied Geoscience & Energy, SEG Technical Program Expanded Abstracts,* pp. 161–164, SEG.

University of Wyoming, 2021. http://weather.uwyo.edu/upperair/sounding.html

van Wyk de Vries, B. & Francis, P., 1997. Catastrophic collapse at stratovolcanoes induced by gradual volcano spreading, *Nature,* **387,** 387–390

Voight, B., 2000. Structural stability of andesite volcanoes and lava domes, *Phil. Trans. R. Soc. A,* **358,** 1663–1703

Voight, B. & Elsworth, D., 1997. Failure of volcano slopes, *Geotechnique,* **47,** 1–31

Voight, B., Janda, R.J. & Glicken, H., 1983. Nature and mechanics of the mount St Helens rockslide—avalanche of 18 May 1980, *Géotechnique,* **20,** 243–273

Watters, R., Zimbelman, D., Bowman, S. & Crowley, J.K., 2000. Rock mass strength assessment and significance to edifice stability, Mount Rainier and Mount Hood, Cascade Range volcanoes, *Pure appl. Geophys.,* **157,** 957–976.

Yamamoto, T., Takarada, S. & Suto, S., 1993. Pyroclastic flows from the 1991 eruption of Unzen volcano Japan, *Bull. Volcanol.,* **55,** 166–175

Yilmaz, T.I. *et al.* 2021. Rapid alteration of fractured volcanic conduits beneath Mt Unzen, *Bull. Volcanol.* **83,** 34

Zhang, Z.-X., Enqvist, T., Holma, M. & Kuusiniemi, P., 2020. Muography and its potential applications to mining and rock engineering, *Rock Mech. Rock Eng.,* **53,** 4893–4907